Structure of low-lying states of ^{12}C and $^{13}_{\Lambda}$C in a beyond-mean-field approach

Huai-Tong Xue (薛怀通),[1] Q. B. Chen (陈启博),[1] Ji-Wei Cui (崔继伟),[2] C.-F. Chen (陈超锋),[3] H.-J. Schulze,[4] and Xian-Rong Zhou (周先荣)[1,*]

[1]*Department of Physics, East China Normal University, Shanghai 200241, China*

[2]*School of Physics and Optoelectronic Engineering, Xidian University, Xi'an 710071, China*

[3]*School of Physics Science and Engineering, Tongji University, Shanghai 200092, China*

[4]*INFN Sezione di Catania, Dipartimento di Fisica, Universitá di Catania, Via Santa Sofia 64, 95123 Catania, Italy*

(Received 15 November 2023; accepted 2 February 2024; published 23 February 2024)

Based on the beyond-mean-field Skyrme-Hartree-Fock model, we investigate the energy spectra and possible cluster structure in ^{12}C and its Λ hypernucleus $^{13}_{\Lambda}$C. The up-to-date Skyrme-type $N\Lambda$ interaction SLL4 and the reduced NN interaction SGII are employed. Low-lying energy spectra of ^{12}C, including the lowest five 0^+ states, are predicted and discussed in detail, and found in good agreement with experimental results. The electric quadrupole transition rates and the monopole matrix elements between the 0^+ states are also examined. Although typical cluster structures for the 0^+_2 and 0^+_3 states are absent, a linear-chain-like 3α structure is found for the 0^+_4 state. An energy spectrum including both the positive- and negative-parity levels is also given and structures of the corresponding hypernuclear states are discussed in detail. Impurity effects of a Λ_s or Λ_p hyperon on the nuclear core states of $^{13}_{\Lambda}$C are demonstrated by the change of collective wave functions.

DOI: 10.1103/PhysRevC.109.024324

I. INTRODUCTION

It is well known that ^{12}C is a typical nucleus in which several kinds of intrinsic structures exist and compete with each other, including the shell structure, triangle-like 3α structure, and linear 3α structure [1,2]. Thus it has for a long time been drawing attention from both experiments and theoretical investigations. Besides, in the hypernuclear sector, $^{13}_{\Lambda}$C is observed and the interactions between a Λ hyperon and various core states of ^{12}C are also an interesting topic [3,4].

In experiments, besides the ground state of ^{12}C with a shell structure, the 0^+_2 'Hoyle state' has been predicted and observed for a long time [5,6] and is generally regarded as a triangle-like 3α cluster state [7]. In recent years, the 0^+_3 and 0^+_4 states were also observed at around 10 MeV with respect to the ground state [8]. The 0^+_3 state was predicted to have a higher nodal structure than the Hoyle state, while the 0^+_4 state was expected to have a linear-like 3α structure [7,9,10]. In the past 40 years, observations of the corresponding hypernucleus $^{13}_{\Lambda}$C have also achieved great progress, and its energy spectrum including both positive- and negative-parity states was well established [11,12], which allows to study in detail the impurity effects caused by a s- or p-orbital Λ hyperon onto the core states of ^{12}C.

Quite a few theoretical studies have made efforts to understand the structures of quantum states in ^{12}C, especially the α-cluster structures. For example, some studies were based on models or assumptions, including limiting cases like linear chains [13,14], equilateral triangles [15], and a Bose-Einstein condensate [16]. Also *ab initio* calculations have been performed, investigating the structure and rotations of the Hoyle state in ^{12}C [17]. Special attention should be paid to the few-body cluster models [10,16,18,19] and the antisymmetrized molecular dynamics (AMD) method [7,20], both of which successfully reproduced the energy spectra of ^{12}C and also $^{13}_{\Lambda}$C. Regarding $^{13}_{\Lambda}$C, several theoretical studies focus on how the structure of ^{12}C is affected by the Λ hyperon. These models include the shell model [21], four-body cluster model [18,19], AMD [20], and the α-condensate model [22].

In recent years, nuclear mean-field (MF) energy-density functionals (EDFs) [23–27] and beyond-MF approaches [28–31] were extended to hypernuclei. One advantage of a hypernuclear EDF is that it is less hindered by computational burdens and allows to study medium or heavy hypernuclei. Another advantage is that the (beyond-)MF approaches treat nucleons and hyperons on the same footing, and α clusters are not assumed *a priori*. Recent research [32,33] showed that the beyond-MF models are able to provide good descriptions of shell and cluster structure of a hypernucleus. Furthermore, the angular momentum projection (AMP) techniques and generator coordinate method (GCM) in these models restore the rotational symmetry and enable the mixing of different configurations, which provides a comprehensive reproduction of hypernuclear energy spectra. In this current work, a Skyrme-type EDF of NN and $N\Lambda$ interactions will be employed in the beyond-MF approach to describe low-lying states of ^{12}C and $^{13}_{\Lambda}$C, and to analyze the rearrangement effects of a Λ $1s$ or $1p$ hyperon on the core states.

This paper is organized as follows. Section II reviews briefly the formalism of the beyond-SHF model. Section III

*xrzhou@phy.ecnu.edu.cn

presents the results and discussions, and in Sec. IV we summarize the work.

II. THEORETICAL FRAMEWORK

The hypernuclear states are given by a superposition of projected MF wave functions onto exact angular momentum J:

$$\left|\Psi_\alpha^{JM}\right\rangle = \sum_\beta F_\alpha^J(\beta)\hat{P}_{MK}^J\left|\Phi^{(N\Lambda)}(\beta)\right\rangle, \tag{1}$$

where $F_\alpha^J(\beta)$ is a weight function, and $\hat{P}_{MK}^J$ is the AMP operator with $K = K_{\rm core} + K_\Lambda$ representing the projection of angular momentum J^π onto the intrinsic z axis.

The hypernuclear MF wave function obtained from a SHF calculation with a quadrupole constraint is given by

$$\left|\Phi^{(N\Lambda)}(\beta)\right\rangle = |\Phi^N(\beta)\rangle \otimes |\Phi^\Lambda\rangle\,, \tag{2}$$

where $|\Phi^N(\beta)\rangle$ and $|\Phi^\Lambda\rangle$ are intrinsic wave functions of the nuclear core and of the Λ hyperon, respectively. More specifically, the hyperon wave function for single-Λ hypernuclei is

$$|\Phi^\Lambda\rangle = \varphi_s(\Lambda) \tag{3}$$

and

$$|\Phi^N(\beta)\rangle = \prod_{k>0}(u_k + v_k a_k^+ a_{\bar{k}}^+)|{\rm HF}\rangle \tag{4}$$

is a Bardeen-Cooper-Schrieffer (BCS) state obtained from the nuclear SHF + BCS calculation with density-dependent δ interaction [34], constrained to an axially deformed shape given by the deformation parameter β, which is proportional to the quadrupole moment,

$$\beta = \frac{4\pi}{3A_cR_c^2}\langle\Phi^N(\beta)|r^2Y_{20}|\Phi^N(\beta)\rangle\,, \tag{5}$$

where A_c is the mass number of the core nucleus, and $R_c \equiv 1.2A_c^{1/3}$ fm.

To obtain the eigenstate $|\Psi_\alpha^{JM}\rangle$, each weight $F_\alpha^J(\beta)$ in Eq. (1) is determined by the Hill-Wheeler-Griffin equation [35],

$$\sum_{\beta'}\left[H_{KK}'^J(\beta,\beta') - E_\alpha^J N_{KK}^J(\beta,\beta')\right]F_\alpha^J(\beta') = 0\,, \tag{6}$$

in which the corrected Hamiltonian and norm elements are given by

$$H_{KK'}'^J(\beta,\beta') = \langle\Phi^{(N\Lambda)}(\beta')|\hat{H}'\hat{P}_{KK'}^J|\Phi^{(N\Lambda)}(\beta)\rangle\,, \tag{7}$$

$$N_{KK'}^J(\beta,\beta') = \langle\Phi^{(N\Lambda)}(\beta')|\hat{P}_{KK'}^J|\Phi^{(N\Lambda)}(\beta)\rangle. \tag{8}$$

The corrected Hamiltonian $\hat{H}'$ is defined as

$$\hat{H}' = \hat{H} - \lambda_p(\hat{N}_p - Z) - \lambda_n(\hat{N}_n - N)\,, \tag{9}$$

where the Hamiltonian $\hat{H}$ is determined by the hypernuclear EDF, and the last two terms account for the fact that the projected wave function does not provide the correct number of particles on average [36]. The projected energy curve onto a specific angular momentum is derived as

$$E_{JK}(\beta) = \frac{H_{KK}'^J(\beta,\beta)}{N_{KK}^J(\beta,\beta)}\,. \tag{10}$$

Since the projected states do not form an orthogonal basis, $F_\alpha^J(\beta)$ are nonorthogonal functions [37], and orthogonal collective wave functions are constructed as

$$g_\alpha^J(\beta) = \sum_{\beta'}[\mathcal{R}^{\frac{1}{2}}]^J(\beta,\beta')F_\alpha^J(\beta')\,, \tag{11}$$

which are weights of the natural states in the collective subspace [35], and where

$$[\mathcal{R}^{\frac{1}{2}}]^J(\beta,\beta') = \sum_k \sqrt{n_k}w_k(\beta)w_k^*(\beta') \tag{12}$$

with the eigenfunctions w_k and eigenvalues n_k of the norm operator, Eq. (8), in the projected space. The average deformation

$$\bar{\beta}_\alpha^J = \sum_\beta \left|g_\alpha^J(\beta)\right|^2\beta \tag{13}$$

reflects the shape of the dominant configurations in the ground or excited state and indicates the band structure [38].

Given the weight function $F_\alpha^J(\beta)$, the root-mean-square (rms) radius is defined as

$$R_{\rm rms}^{J\alpha} = \sqrt{\sum_{\beta\beta'}F_\alpha^J(\beta')^*F_\alpha^J(\beta)\langle\Phi^{(N\Lambda)}(\beta')|r^2\hat{P}_{KK}^J|\Phi^{(N\Lambda)}(\beta)\rangle} \tag{14}$$

with $r^2 = \frac{1}{A}\sum_k r_k^2$, and the reduced $E2$ transition rate is derived as

$$B(E2, J_\alpha^+ \to J_{\alpha'}'^+) = \frac{1}{2J+1}|\langle J_{\alpha'}'^+||\hat{Q}_2||J_\alpha^+\rangle|^2\,, \tag{15}$$

where the reduced matrix element is

$$\langle J_{\alpha'}'^+||\hat{Q}_2||J_\alpha^+\rangle = \sqrt{2J'+1}\sum_{M\mu\beta\beta'}F_{\alpha'}^{J'}(\beta')^*F_\alpha^J(\beta)\,C_{JM2\mu}^{J'K'} \times \langle\Phi^{(N\Lambda)}(\beta')|\hat{Q}_{2\mu}\hat{P}_{MK}^J|\Phi^{(N\Lambda)}(\beta)\rangle\,, \tag{16}$$

in which $C_{JM2\mu}^{J'K'}$ denotes the Clebsh-Gordon coefficients, and $\hat{Q}_{2\mu} = \sum_k e_k r_k^2 Y_{2\mu}(\varphi_k,\theta_k)$ is the electric quadrupole transition operator [39], where e_k is the charge of the kth nucleon and r_k is its position relative to the center of mass of the nucleus. Bare charges are used in this calculation, i.e., $e_p = e$ and $e_n = e_\Lambda = 0$.

Electric monopole ($E0$) transitions are calculated from the off-diagonal matrix elements of the $E0$ operator. The corresponding diagonal matrix elements are directly related to the rms charge radii that provide signatures of shape changes in nuclei. The $E0$ operator can be expressed in terms of single-nucleon degrees of freedom as $\hat{T}(E0) = \sum_k e_k r_k^2$ [40,41]. The absolute $E0$ transition strength is defined as

$$\rho^2(E0, J_{\alpha'}^+ \to J_\alpha^+) = \left|\frac{\langle J_{\alpha'}^+|\hat{T}(E0)|J_\alpha^+\rangle}{eR_c^2}\right|^2\,, \tag{17}$$

where $R_c \equiv 1.2A_c^{1/3}$ fm is the nuclear radius and $J = 0, 1/2$ for nuclei and hypernuclei, respectively. In the AMP + GCM

framework, the $E0$ matrix element is

$$\langle J^+_{\alpha'}|\hat{T}(E0)|J^+_{\alpha}\rangle = \sum_{\beta\beta'} F^J_{\alpha'}(\beta')^* F^J_{\alpha}(\beta) \times \left\langle \Phi^{(N\Lambda)}(\beta')\middle|\hat{T}(E0)\hat{P}^J_{KK}\middle|\Phi^{(N\Lambda)}(\beta)\right\rangle. \tag{18}$$

Regarding the interactions employed in this work, we adopt the NN Skyrme force SGII [42], in which the NN spin-orbit (s.o.) interaction is reduced to 70% [43,44] in order to reproduce the oblate shape of ^{12}C in the MF calculation. The strength of the density-dependent pairing interaction is $V = -410$ MeV fm^3 for both protons and neutrons, and a smooth pairing energy cutoff of 5 MeV above the Fermi level is used [43,45].

For the ΛN interaction, we use the SLL4 Skyrme force [26,27], which provides the best overall fit of all current single-Λ hypernuclear data. The corresponding energy-density functional is of the form

$$\begin{aligned}\varepsilon_\Lambda = {} & \frac{\tau_\Lambda}{2m_\Lambda} + a_0\rho_\Lambda\rho_N + a_3\rho_\Lambda\rho_N^2 \\ & + a_1(\rho_\Lambda\tau_N + \rho_N\tau_\Lambda) - a_2(\rho_\Lambda\Delta\rho_N + \rho_N\Delta\rho_\Lambda)/2 \\ & - a_4(\rho_\Lambda\nabla\cdot\boldsymbol{J}_N + \rho_N\nabla\cdot\boldsymbol{J}_\Lambda)\,,\end{aligned} \tag{19}$$

where the last term is the ΛN s.o. part. For convenience we repeat here the parameter values [27]: $a_{0,1,2,3} = [-322.0, 15.75, 19.63, 715.0]$ (in appropriate units for ρ given in fm^{-3} and ε in MeV fm^{-3}), whereas the small s.o. term is neglected in this work.

III. RESULTS AND DISCUSSION

Figure 1 shows the potential energy surfaces (PESs) of ^{12}C and $^{13}_{\Lambda}$C, comparing results of MF calculations (thin curves) and AMP onto specific J^π (thick curves). It is seen that the MF PES of ^{12}C (thin solid black curve) has a minimum energy of 92.6 MeV at the quadrupole deformation $\beta \approx -0.36$, which agrees well with the observed data 92.16 MeV [46]. The projected PES of ^{12}C with $J^\pi = 0^+$ (solid thick black curve) is calculated according to Eq. (10), and has two obvious minima with $E = -97.1$ MeV and $E = -95.8$ MeV that are, respectively, oblately ($\beta = -0.58$) and prolately ($\beta = 0.58$) deformed.

The effect of the added Λ in $^{13}_{\Lambda}$C is basically a downward shift of the PES by about 12 MeV in both MF and AMP (red curves). The MF energy minimum is now located at $\beta = -0.31$ with energy -104.3 MeV, whereas in AMP the two energy minima are at $\beta = -0.53$ and 0.58 with energies of -108.7 and -107.7 MeV. The deformation corresponding to the minima is slightly reduced by the Λ hyperon, which is well known as shrinkage effect [31,47–51].

The energies E^J_α, Eq. (6), and average deformations $\bar{\beta}$, Eq. (13), of the various 0^+ and $1/2^+$ states are also indicated in the plot and listed in Table I, and will be discussed in detail in the following. Here, we just note that the ^{12}C ground-state energy in AMP is $-E(0^+_1) = 97.6$ MeV, substantially larger than the experimental value 92.16 MeV [46]. The energy gain

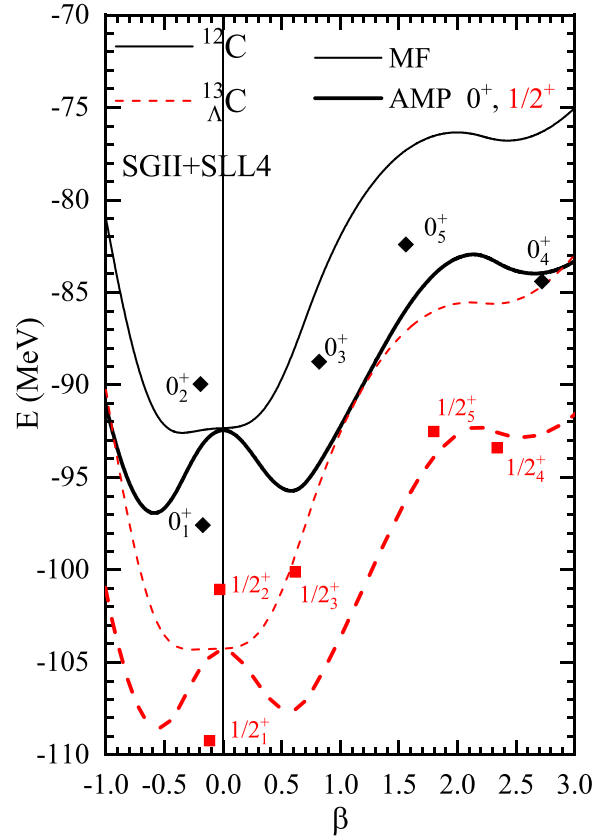

FIG. 1. The potential energy surfaces (PESs) of MF (thin curves) and AMP states (thick curves): 0^+ states for ^{12}C (solid black curves), $1/2^+$ for $^{13}_{\Lambda}$C (dashed red curves). The markers indicate the energy, Eq. (6), and average deformation, Eq. (13), of the excited states 0^+_α and $1/2^+_\alpha$, $\alpha = 1, \ldots, 5$.

is caused by the restoration of rotational symmetry and the shape fluctuation effect that arises from configuration mixing.

The removal energy of the Λ $1s$ state is $B_\Lambda = E(0^+_1) - E(1/2^+_1) = 11.6$ MeV, in fair agreement with experimental values 11.7 ± 0.12 MeV (emulsion) [52], 12.0 ± 0.2 (π^+, K^+) [3,53], 11.0 ± 0.4 (K^-, π^-) [54,55], which unfortunately do not agree very well.

TABLE I. The excitation energies E, rms charge radii R_c, and average deformations $\bar{\beta}$ of the 0^+, 2^+, 4^+ states of ^{12}C and the $1/2^+$, $3/2^+$, $5/2^+$, $7/2^+$, $9/2^+$ states of $\Lambda(1s)$ $^{13}_{\Lambda}$C.

^{12}C				$^{13}_{\Lambda}$C			
	E [MeV]	R_c [fm]	$\bar{\beta}$		E [MeV]	R_c [fm]	$\bar{\beta}$
0^+_1	0	2.60	−0.17	$1/2^+_1$	−11.64	2.57	−0.12
0^+_2	7.62	2.58	−0.19	$1/2^+_2$	−3.47	2.56	−0.03
0^+_3	8.84	2.60	0.82	$1/2^+_3$	−2.53	2.57	0.62
0^+_4	13.17	3.32	2.72	$1/2^+_4$	4.19	3.19	2.34
0^+_5	15.17	2.86	1.59	$1/2^+_5$	5.07	2.92	1.80
2^+_1	3.57	2.62	−0.52	$(3,5)/2^+_1$	−7.76	2.58	−0.48
4^+_1	12.60	2.63	−0.59	$(7,9)/2^+_1$	1.67	2.60	−0.57

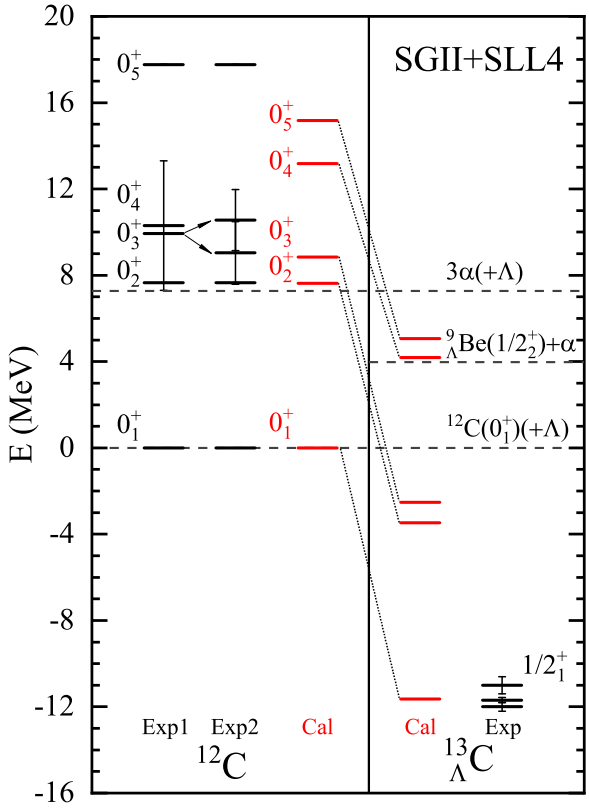

FIG. 2. Energy levels of ^{12}C(0^+) (left columns) and $^{13}_{\Lambda}$C($1/2^+$) (right columns). The broad resonance state 0^+_4 at 10.3 ± 3 MeV [46] in the first column is in the second column decomposed into 0^+_3 and 0^+_4 states at 9.04 ± 1.45 and 10.56 ± 1.42 MeV, respectively [8]. Experimental $^{13}_{\Lambda}$C($1/2^+_1$) results are from Refs. [52,53,55]. The thresholds of various decay channels are also indicated.

A. ^{12}C states

In the first three columns of Fig. 2, we show again the 0^+ states obtained with the SHF + AMP + GCM approach, in comparison with experimental data [8,46]. The excitation energy of the 0^+_2 Hoyle state is 7.62 MeV, which perfectly agrees with the experimental value of 7.65 MeV. The result for the 0^+_3 state is 8.84 MeV, reasonably close to the experimental values of 9.93 MeV [46] and 9.04 MeV [8]. But the theoretical 0^+_4 state at 13.17 MeV differs substantially from the experimental values of 10.56 ± 1.42 MeV [8] and 10.3 ± 3 MeV [46], while the 0^+_5 state at 15.17 MeV is lower than the experimental value by 2.5 MeV. However, also the often-used cluster models THSR [56,57] and OCM [58–60] have difficulty in describing the excitation energy of $0^+_{3,4}$ and differ for 0^+_4 by approximately 2 MeV.

In order to understand better the (cluster) structure of these states, we plot their nuclear density distributions in Fig. 3. The ground state of ^{12}C has a shell-model-like structure. The gas-like structure of three α clusters in the 0^+_2 Hoyle state [16,61,62] is absent in this work. Accordingly, also the 0^+_3 state is without cluster structure, which is considered to have a composition similar to that of the Hoyle state, and to be excited from that with a large monopolar transition strength [22]. On the other hand, the 0^+_4 state features a very obvious linear-chain-like structure of three α clusters, as in other theoretical approaches [7,9,10]. The 0^+_5 state forms a prolate shape without apparent cluster structure. In the future, improved modeling, such as the idea given in Ref. [63], may provide both 0^+_2 and 0^+_3 cluster structures.

Thus, for the $0^+_{2,3}$ states the SHF + AMP + GCM method predicts excitation energies in good agreement with experiment, but does not evidence typical cluster structures, and their calculated rms radii are much smaller than those

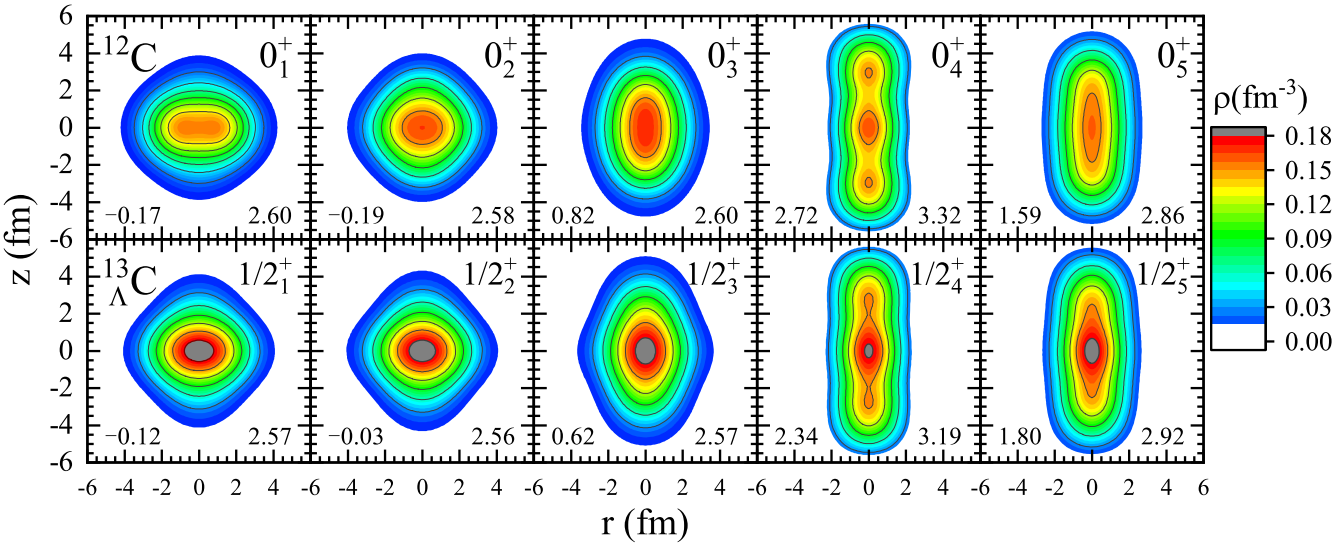

FIG. 3. Two-dimensional nuclear-matter density distributions of the first five 0^+ states in ^{12}C (top row) and of the corresponding $1/2^+$ states in $^{13}_{\Lambda}$C (bottom row). The average quadrupole deformation $\bar{\beta}$ and the charge radius R_c (in fm) are also indicated in the lower left and right corners, respectively.

calculated by THSR [9] and OCM [22], namely 2.58 and 2.60 fm, compared to 3.7/4.2 fm (THSR) and 4.7/5.6 fm (OCM), respectively. Their radii are also smaller than those of the 0^+_4 and 0^+_5 states, 3.32 and 2.86 fm. These results are also listed in Table I.

We discuss now the differences between the results of this work and those of other (cluster) models.

First, regarding that the Hoyle state might be modeled as a dilute self-bound gas of three bosonic α particles, similar to a Bose-Einstein condensate [10], it is impossible to accurately characterize the density distribution of such a structure in a system that only considers quadrupole deformation. It might be possible to improve the modeling of this state by extending the space of CGM reference states and including possible octupole, etc., deformation of the nucleus.

Second, some studies have discussed the possibility of relativistic and nonrelativistic density functional theories to describe cluster structures [64–66], and point out that this is closely related to the depth of the MF potential. They also suggest that the relativistic density functional, due to its deep potential field, yields a more pronounced cluster structure than the SHF with a shallow average potential field. Therefore, it is possible that a relativistic beyond-MF method may also result in a more pronounced cluster structure of the Hoyle state.

Third, antisymmetrized quasicluster model (AQCM) results, which include s.o. interactions between α clusters, indicate that those interactions can drive the breaking of α clusters and lower the 0^+_1-state energy of ^{12}C [67]. The distance between α clusters in that state is significantly reduced by 0.5 fm to 1.0 fm compared to the pure cluster model. Since the SHF + AMP + GCM method used in this work self-consistently includes s.o. interactions between nucleons, it is reasonable to also obtain α-cluster breaking in the 0^+_1 state of ^{12}C and to explain why the rms radius calculated by OCM is larger than in this work. However, Ref. [67] does not investigate whether cluster destruction occurs also in the Hoyle state.

Moreover, the AQCM also shows that the s.o. interaction does not destroy the cluster structure in ^{8}Be [67]. Also in Ref. [32], using the same SHF + AMP + GCM method as this work, the cluster structure of ^{8}Be is not broken. Therefore, the results of SHF + AMP + GCM and AQCM are consistent in some aspects.

B. States of the configuration $^{12}\mathrm{C}\otimes\Lambda_s$

Figure 2 shows the first five $1/2^+$ states based on the configuration $^{12}\mathrm{C}\otimes\Lambda_s$, of which the $1/2^+_{1,2,3}$ states are bound states, while $1/2^+_{4,5}$ are unbound, i.e., resonances above the $^{12}\mathrm{C}(0^+_1)+\Lambda$ threshold. Comparing the energy levels of ^{12}C and $^{13}_{\Lambda}$C in Fig. 2 and the corresponding density distributions in Fig. 3 one concludes that the structure of the first five $1/2^+$ states is similar to that of the corresponding 0^+ states. This similarity is due to the fact that the s-orbit Λ is spherically distributed (or mildly deformed) and thus does not change the shape of the nuclear core dramatically.

This is also demonstrated in Fig. 4 by the weights of the natural states in the collective subspace, Eq. (11). Again

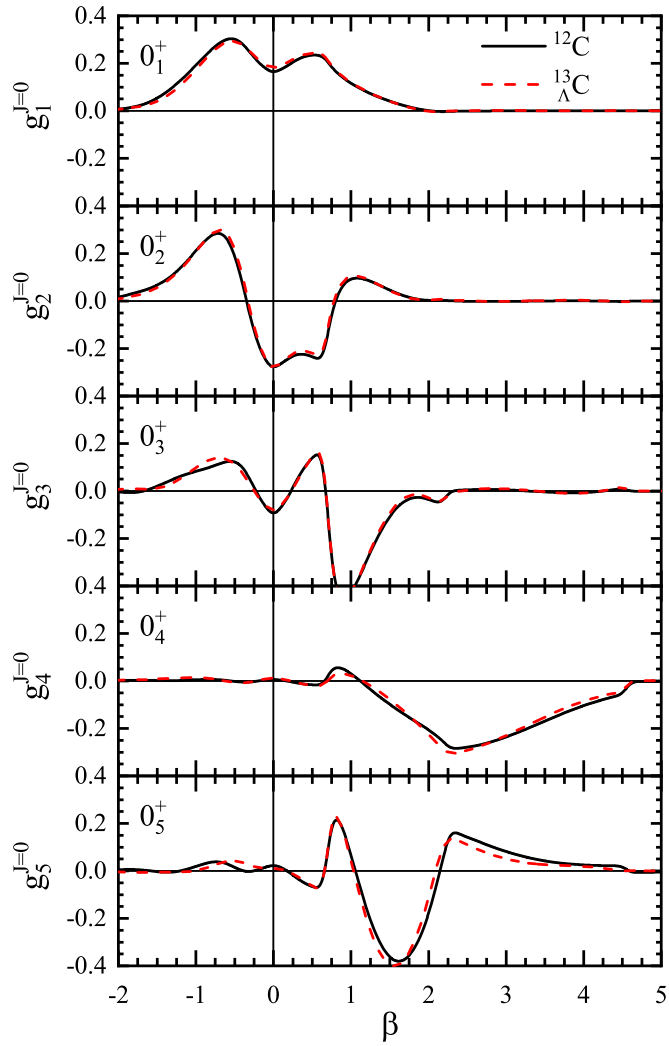

FIG. 4. Weights of the natural states in the collective subspace, $g^{J=0}_\alpha$, Eq. (11), for the first five GCM states of $^{12}\mathrm{C}(0^+)$ and $^{13}_{\Lambda}\mathrm{C}(1/2^+)$.

the weights of the $1/2^+$ states are similar to those of the corresponding 0^+ states. This is different from the results of THSR [57], where each of the first four $1/2^+$ states of $^{13}_{\Lambda}$C is a mixture of several 0^+ states of ^{12}C.

Table I lists the rms charge radii of the first five 0^+ states of ^{12}C and the first five $1/2^+$ states of $^{13}_{\Lambda}$C. The radii of 0^+_4 and $1/2^+_4$ are significantly larger than those of the other states, consistent with the nuclear density distributions shown in Fig. 3. One also observes the well-known shrinkage effect of the Λ [31,47–51], where the added $1s$ Λ causes a contraction of the density distribution and a reduction of the deformation. This contributes to driving the breaking of the cluster structure in the hypernucleus, which is consistent with the conclusion of the AQCM [67].

In Table II we list the $E2$ transition probabilities within the ground bands of ^{12}C and $^{13}_{\Lambda}$C. Due to the splitting of angular momentum into $J\pm 1/2$, each of the $B(E2)$ values of the core nucleus has two counterparts in the hypernucleus, which are both listed. The addition of one Λ reduces slightly the $B(E2)$

TABLE II. Transition rates $B(E2)$, Eq. (15), (in units of $e^2\text{fm}^4$) and the ratios Γ_B, Eq. (20). Experimental value [46] in brackets.

^{12}C		$^{13}_{\Lambda}$C		
$J_i \to J_f$	$B(E2)$	$J_i \to J_f$	$B(E2)$	Γ_B
$2^+_1 \to 0^+_1$	11.5 (7.6)	$3/2^+_1 \to 1/2^+_1$	10.7	0.93
		$5/2^+_1 \to 1/2^+_1$	10.7	0.93
$4^+_1 \to 2^+_1$	17.8	$7/2^+_1 \to 3/2^+_1$	15.1	0.85
		$9/2^+_1 \to 5/2^+_1$	16.8	0.94

values and this shrinkage effect is characterized by [28]

$$\Gamma_B = \frac{B\left(E2, J_i^+ \to J_f^+; {}^{13}_{\Lambda}\text{C}\right)}{B\left(E2, J_i^+ \to J_f^+; {}^{12}\text{C}\right)}, \tag{20}$$

also listed in the table. The $E2$ transition probabilities are proportional to R_c^4 and to β^2 [31]. Both the shrinkage of the nuclear size indicated by R_c and the reduction of the quadrupole deformation $\bar{\beta}$, shown in Table I and Fig. 3, thus contribute to the overall reduction of $B(E2)$.

It is also interesting to examine, in Table III, the monopole matrix elements between the 0^+ states, Eq. (17), i.e., the off-diagonal matrix elements of the $E0$ operator. They act as a spectroscopic fingerprint for the presence of shape mixing in a region of nuclei [40]. The transition strength between some states is very small, $\approx 10^{-4}$, which indicates a very weak correlation. The strongest $E0$ transitions are $0^+_2 \to 0^+_1$ ($1/2^+_2 \to 1/2^+_1$) and $0^+_5 \to 0^+_4$ ($1/2^+_5 \to 1/2^+_4$). This reflects the great similarity between these excited pair states, which can also be noted from the density distributions in Fig. 3 and from the weights of the natural states in the collective subspace given in Fig. 4. In Ref. [68] the 0^+_3 state was predicted as a breathing mode, excited by a strong monopole transition from the 0^+_2 Hoyle state. This cluster feature is absent in this work, where the $0^+_3 \to 0^+_2$ strength is fairly small instead.

C. States of the configuration $^{12}\text{C} \otimes \Lambda_p$

Besides the positive-parity states based on the configuration $^{12}\text{C} \otimes \Lambda_s$, negative-parity states are also observed and attributed to the configuration $^{12}\text{C} \otimes \Lambda_p$ [12]. Figure 5

TABLE III. $\rho^2(E0, J^+_{\alpha_i} \to J^+_{\alpha_f})$ values between ^{12}C 0^+_α states and $^{13}_{\Lambda}$C $1/2^+_\alpha$ states.

$\alpha_i \to \alpha_f$	$^{12}\text{C}(0^+)$	$^{13}_{\Lambda}\text{C}(1/2^+)$
$2 \to 1$	1.77×10^{-1}	1.34×10^{-1}
$3 \to 1$	1.15×10^{-3}	1.70×10^{-2}
$4 \to 1$	4.66×10^{-5}	7.40×10^{-4}
$5 \to 1$	5.34×10^{-4}	1.76×10^{-3}
$3 \to 2$	3.54×10^{-4}	2.05×10^{-4}
$4 \to 2$	3.28×10^{-4}	8.61×10^{-3}
$5 \to 2$	6.27×10^{-3}	7.01×10^{-3}
$4 \to 3$	1.02×10^{-2}	1.23×10^{-2}
$5 \to 3$	4.12×10^{-2}	1.59×10^{-2}
$5 \to 4$	3.12×10^{-1}	9.07×10^{-2}

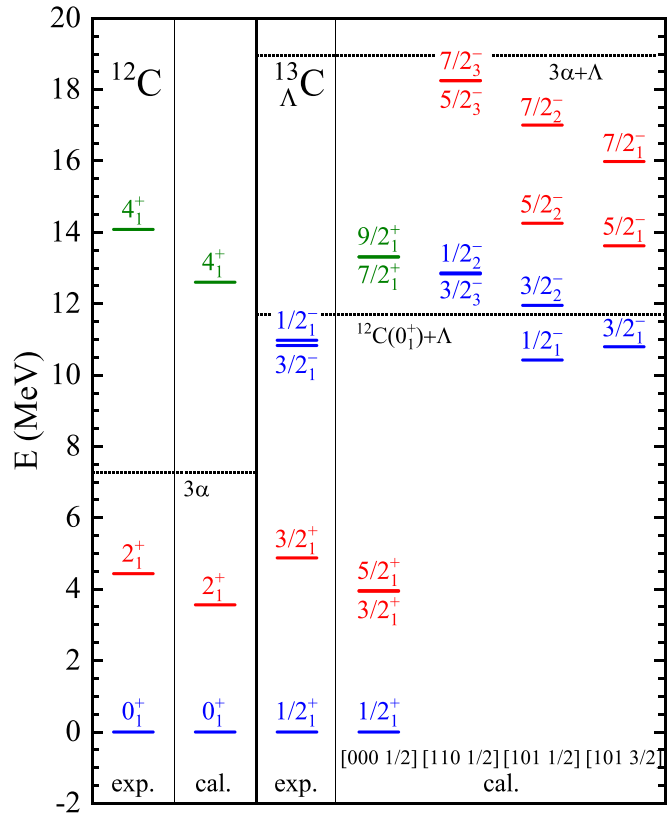

FIG. 5. The energy levels of ^{12}C (left side) and $^{13}_{\Lambda}$C (right side), comparing experimental and theoretical values. Colors indicate the predominant core configurations.

shows the predicted energy spectra of $^{13}_{\Lambda}$C including both positive- and negative-parity bands. The three negative-parity bands correspond to the configurations $^{12}\text{C} \otimes \Lambda$[110 1/2], $^{12}\text{C} \otimes \Lambda$[101 1/2], and $^{12}\text{C} \otimes \Lambda$[101 3/2], where Nilsson notations indicate the Λ orbits. There are two pairs of states with $J^\pi = (3/2^-, 1/2^-)$. The first pair, $(3/2^-_3, 1/2^-_2)$, located at 12.8 MeV, is the band head of the configuration $^{12}\text{C} \otimes \Lambda$[110 1/2]. The second pair, $(3/2^-_1, 1/2^-_1)$, of bound states at $\approx$10.6 MeV, is very close to the observed s.o. doublet [12]. Those two states are band heads of the configurations $^{12}\text{C} \otimes \Lambda$[101 3/2] and $^{12}\text{C} \otimes \Lambda$[101 1/2], respectively. However, the predicted order of the states is opposite to the observed one [30].

A hypernuclear state of $^{13}_{\Lambda}$C could approximately be regarded as a ^{12}C core coupled with a single Λ or as a mixture of several such configurations. However, in current model it is difficult to quantitatively calculate the contribution of each core state to a certain hypernuclear state, contrary to the H-THSR model [57], for example. To analyze the constitution of the low-lying hypernuclear states given in Fig. 5, we show their collective wave functions $g^J_\alpha(\beta)$ in Fig. 6. First, for the ^{12}C core, Fig. 6 shows that the oblate components play dominant roles in the collective wave functions of all three $0^+_1, 2^+_1, 4^+_1$ states. This is also testified in Fig. 7, which shows the corresponding nuclear density distributions of ^{12}C, and indicates that all three states are oblately deformed.

Then, based on these three nuclear core states, we deduce the constituents of the hypernuclear states as follows.

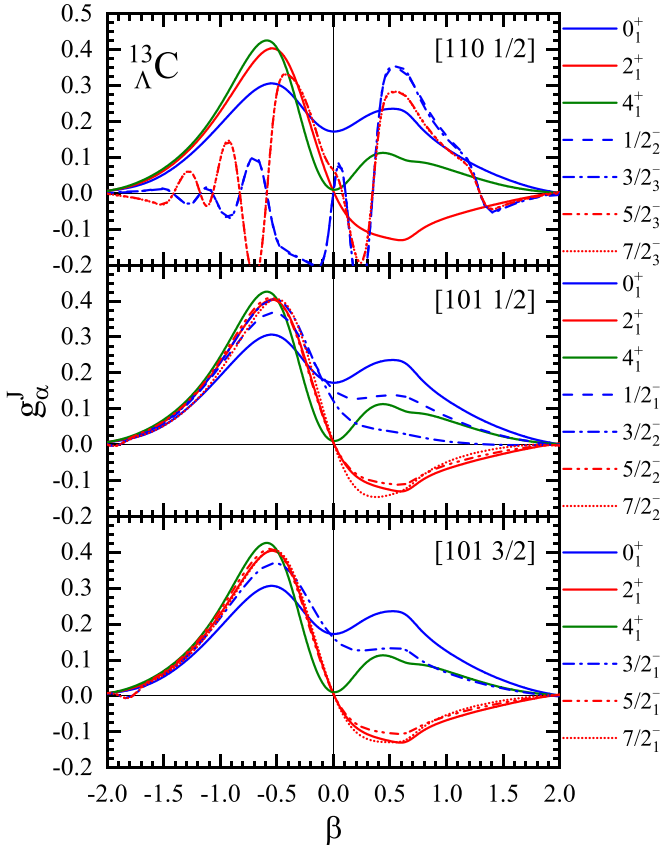

FIG. 6. Collective wave functions of the (hyper)nuclear states shown in Fig. 5.

Figure 6 shows g^J_α of the energy levels corresponding to the $^{12}\mathrm{C}\otimes\Lambda$[110 1/2], $^{12}\mathrm{C}\otimes\Lambda$[101 1/2], and $^{12}\mathrm{C}\otimes\Lambda$[101 3/2] configurations, as in Fig. 5.

For the [101 3/2] channel, only $^{12}\mathrm{C}\otimes\Lambda_{p3/2}$ can play a role in the three energy levels $3/2^-_1$, $5/2^-_1$, $7/2^-_1$, because the quantum number $K = 3/2$ excludes a $^{12}\mathrm{C}\otimes\Lambda_{p1/2}$ contribution. The g^J_α of the $3/2^-_1$ level indicates a mixture of $^{12}\mathrm{C}(0^+_1)\otimes\Lambda_{p3/2}$ and $^{12}\mathrm{C}(2^+_1)\otimes\Lambda_{p3/2}$, while the configuration $^{12}\mathrm{C}(4^+_1)\otimes\Lambda_{p3/2}$ is excluded due to the rules of angular momentum coupling. This is also supported by the results shown in Fig. 7, where one can see that $\bar{\beta} = -0.45$ for the $3/2^-_1$ state, which is between the values of the 0^+_1 and 2^+_1 states of ^{12}C. On the other hand, the g^J_α of the $5/2^-_1$ and $7/2^-_1$ levels are nearly identical to the one of $^{12}\mathrm{C}(2^+_1)$, and thus mainly based on a single configuration $^{12}\mathrm{C}(2^+_1)\otimes\Lambda_{p3/2}$. This is emphasized by the same (red) color in Fig. 5.

Regarding the [101 1/2] states $1/2^-_1, 3/2^-_2, 5/2^-_2, 7/2^-_2$, one can see that g^J_α of the $1/2^-_1$ level is nearly identical to the one of [101 3/2] $3/2^-_1$. But for this channel, both configurations $^{12}\mathrm{C}\otimes\Lambda_{p3/2}$ and $^{12}\mathrm{C}\otimes\Lambda_{p1/2}$ are possible, and thus the latter contribution causes the slightly different energies of the [101 1/2] $1/2^-_1$ and [101 3/2] $3/2^-_1$ states. For the $3/2^-_2$ state, three configurations $^{12}\mathrm{C}(0^+_1)\otimes\Lambda_{p3/2}$, $^{12}\mathrm{C}(2^+_1)\otimes\Lambda_{p3/2}$, and $^{12}\mathrm{C}(2^+_1)\otimes\Lambda_{p1/2}$ are possible. One can see that the g^J_α of the $3/2^-_2$ state is closer to the one of $^{12}\mathrm{C}(2^+_1)$ than the one of the $1/2^-_1$ state, and therefore, the configurations $^{12}\mathrm{C}(2^+_1)\otimes\Lambda_p$ play more important roles in the $3/2^-_2$ state. As the $5/2^-_1$ and $7/2^-_1$ states, also the $5/2^-_2$ and $7/2^-_2$ are mainly based on a single configuration $^{12}\mathrm{C}(2^+_1)\otimes\Lambda_p$.

The wave functions of all [101 1/2] and [101 3/2] states feature predominantly oblate configurations. This is not the case for the $1/2^-_2, 3/2^-_3, 5/2^-_3, 7/2^-_3$ levels built upon a Λ [110 1/2] orbital, which is prolately deformed and stretches also the nuclear core into prolate shape, as shown for the $1/2^-_2$ state in Fig. 7. Thus the original core states of ^{12}C are broken, and it is impossible to find analog hypernuclear states in this channel. The frequent oscillation of g^J_α in Fig. 6 (top panel) also indicates the complex constitution of these hypernuclear states. It is shown that g^J_α of $1/2^-_2$ and $3/2^-_3$ and those of $5/2^-_3$ and $7/2^-_3$, as well as their excitation energies in Fig. 5, are nearly identical, which indicates that these pairs of states ($1/2^-_2$ and $3/2^-_3$, $5/2^-_3$ and $7/2^-_3$) have very similar nuclear cores. Due to their distorted cores, their energies are all higher than those with the same J in Fig. 5.

IV. SUMMARY

Based on the beyond-SHF model with realistic NN and $N\Lambda$ Skyrme interactions, low-lying excited states of ^{12}C and $^{13}_{\Lambda}$C were predicted. The structures of the lowest five $J^\pi = 0^+$ nuclear-core states, and the impurity effects of Λ_s and Λ_p orbitals in the hypernuclear states of $^{13}_{\Lambda}$C were examined in detail.

For ^{12}C, the predicted $0^+_{1,2,3}$ states are in good agreement with the observed ones, while the $0^+_{4,5}$ states deviate from the experimental values by a few MeV, as also in cluster-model calculations. In our framework, although typical cluster structures for 0^+_2 and 0^+_3 are absent, a linear-chain-like 3α structure for 0^+_4 was found.

For $^{13}_{\Lambda}$C, the predicted binding energy of the Λ_s hyperon fits the experimental $1/2^+$ value perfectly. The shrinkage effect of the hyperon is also reproduced by the reduction of $E2$ transition values. We also found that the shrinkage effect of a Λ_s hyperon is not strong enough to damage the structures of the first five 0^+ states in the core nucleus, in contrast with the H-THSR results [57].

Negative-parity energy levels of $^{13}_{\Lambda}$C corresponding to a Λ_p hyperon were also examined. The observed $1/2^-_1$ and $3/2^-_1$ energy levels of the s.o. doublet were predicted as the band heads of the configurations $^{12}\mathrm{C}\otimes\Lambda$[101 1/2] and $^{12}\mathrm{C}\otimes\Lambda$[101 3/2], respectively, with nuclear cores that may be regarded as mixtures of the 0^+_1 and 2^+_1 states of ^{12}C. Unlike the Λ_s hyperon, the [110 1/2] Λ_p orbital causes a severe deformation change of the core nucleus, with a corresponding upshift of the hypernuclear levels.

In the future, explicit incorporation of cluster features into the SHF + AMP + GCM approach would be desirable to improve the joint description of all (hyper)nuclear excitation levels. Also the $N\Lambda$ s.o. force should be included consistently for a more realistic description of related properties.

ACKNOWLEDGMENTS

This work was supported by the National Natural Science Foundation of China under Grants No. 12175071, No. 12205103, and No. 11905165.

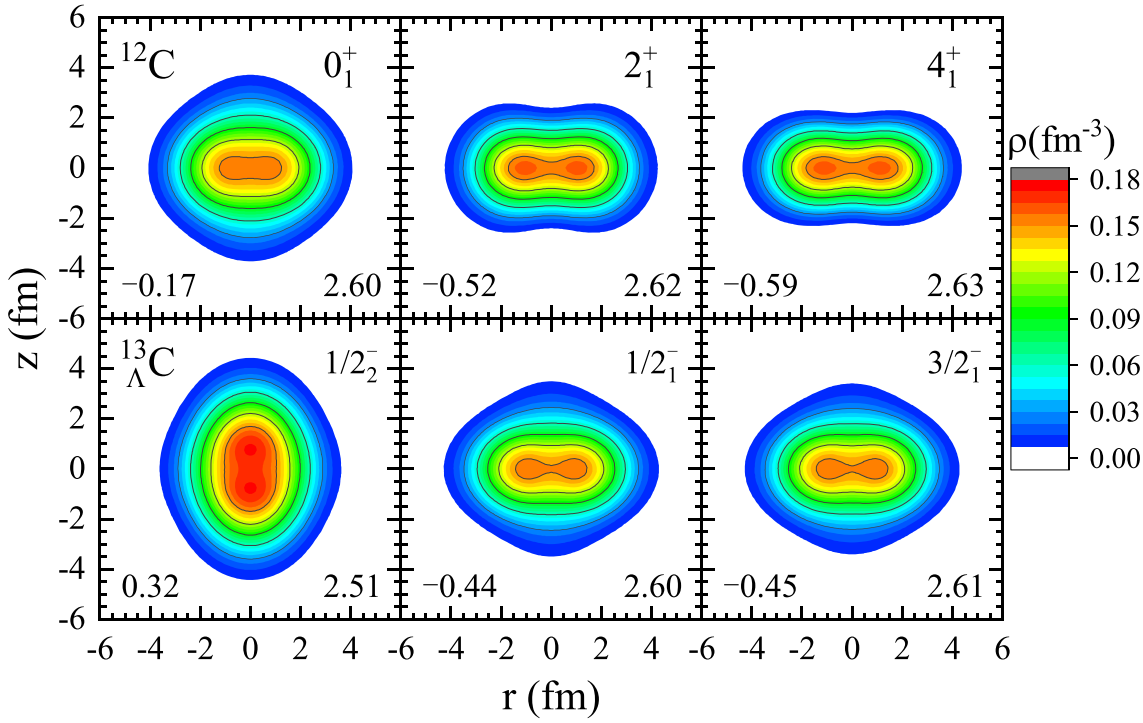

FIG. 7. Same as Fig. 3, but for the 0^+_1, 2^+_1, 4^+_1 states of ^{12}C (top row), and for the band-head states of the three hypernuclear Λ_p configurations in Fig. 5 (bottom row).

[1] Y. Funaki, H. Horiuchi, and A. Tohsaki, Prog. Part. Nucl. Phys. **82**, 78 (2015).
[2] P. Schuck, Y. Funaki, H. Horiuchi, G. Röpke, A. Tohsaki, and T. Yamada, Phys. Scr. **91**, 123001 (2016).
[3] O. Hashimoto and H. Tamura, Prog. Part. Nucl. Phys. **57**, 564 (2006).
[4] E. Hiyama and T. Yamada, Prog. Part. Nucl. Phys. **63**, 339 (2009).
[5] F. Hoyle, Astrophys. J. Suppl. Series **1**, 121 (1955).
[6] C. W. Cook, W. A. Fowler, C. C. Lauritsen, and T. Lauritsen, Phys. Rev. **107**, 508 (1957).
[7] Y. Kanada-En'yo, Prog. Theor. Phys. **117**, 655 (2007).
[8] M. Itoh *et al.*, J. Phys.: Conf. Ser. **436**, 012006 (2013).
[9] Y. Funaki, Phys. Rev. C **94**, 024344 (2016).
[10] M. Chernykh, H. Feldmeier, T. Neff, P. von Neumann-Cosel, and A. Richter, Phys. Rev. Lett. **98**, 032501 (2007).
[11] S. Ajimura *et al.*, Phys. Rev. Lett. **86**, 4255 (2001).
[12] H. Kohri *et al.*, Phys. Rev. C **65**, 034607 (2002).
[13] H. Morinaga, Phys. Rev. **101**, 254 (1956).
[14] P. W. Zhao, N. Itagaki, and J. Meng, Phys. Rev. Lett. **115**, 022501 (2015).
[15] R. Bijker and F. Iachello, Ann. Phys. **298**, 334 (2002).
[16] A. Tohsaki, H. Horiuchi, P. Schuck, and G. Röpke, Phys. Rev. Lett. **87**, 192501 (2001).
[17] E. Epelbaum, H. Krebs, T. A. Lähde, D. Lee, and Ulf-G. Meißner, Phys. Rev. Lett. **109**, 252501 (2012).
[18] E. Hiyama, M. Kamimura, T. Motoba, T. Yamada, and Y. Yamamoto, Prog. Theor. Phys. **97**, 881 (1997).
[19] E. Hiyama, M. Kamimura, T. Motoba, T. Yamada, and Y. Yamamoto, Phys. Rev. Lett. **85**, 270 (2000).
[20] M. Isaka, M. Kimura, A. Dote, and A. Ohnishi, Phys. Rev. C **83**, 044323 (2011).
[21] D. Millener, Nucl. Phys. A **691**, 93 (2001).
[22] Q. Wu, Y. Funaki, and X. Chen, Phys. Rev. C **107**, 014317 (2023).
[23] M. Rayet, Nucl. Phys. A **367**, 381 (1981).
[24] Y. Yamamoto, H. Bandõ, and J. Žofka, Prog. Theor. Phys. **80**, 757 (1988).
[25] Y. Yamamoto, T. Motoba, and T. A. Rijken, Prog. Theor. Phys. Suppl. **185**, 72 (2010).
[26] H.-J. Schulze and E. Hiyama, Phys. Rev. C **90**, 047301 (2014).
[27] H.-J. Schulze, *AIP Conference Proceedings*, Vol. 2130 (AIP Publishing, New York, 2019), p. 020009.
[28] J.-W. Cui, X.-R. Zhou, and H.-J. Schulze, Phys. Rev. C **91**, 054306 (2015).
[29] H. Mei, K. Hagino, and J. M. Yao, Phys. Rev. C **93**, 011301(R) (2016).
[30] J.-W. Cui and X.-R. Zhou, Prog. Theor. Exp. Phys. **2017**, 093D04 (2017).
[31] J.-W. Cui, X.-R. Zhou, L.-X. Guo, and H.-J. Schulze, Phys. Rev. C **95**, 024323 (2017).
[32] W.-Y. Li, J.-W. Cui, and X.-R. Zhou, Phys. Rev. C **97**, 034302 (2018).
[33] H. J. Xia, X. Y. Wu, H. Mei, and J. M. Yao, Sci. China Phys. Mech. Astron. **66**, 252011 (2023).

[34] M. Bender, K. Rutz, P. G. Reinhard, and J. A. Maruhn, Eur. Phys. J. A **8**, 59 (2000).
[35] P. Ring and P. Schuck, *The Nuclear Many Body Problem* (Springer-Verlag, Berlin, 1980).
[36] P. Bonche, J. Dobaczewski, H. Flocard, P.-H. Heenen, and J. Meyer, Nucl. Phys. A **510**, 466 (1990).
[37] H. Mei, K. Hagino, J. M. Yao, and T. Motoba, Phys. Rev. C **91**, 064305 (2015).
[38] M. Bender, P. Bonche, and P.-H. Heenen, Phys. Rev. C **74**, 024312 (2006).
[39] J. Dobaczewski *et al.*, Comput. Phys. Commun. **180**, 2361 (2009).
[40] J. Wood, E. Zganjar, C. De Coster, and K. Heyde, Nucl. Phys. A **651**, 323 (1999).
[41] Z. P. Li, T. Nikšić, D. Vretenar, and J. Meng, Phys. Rev. C **80**, 061301(R) (2009).
[42] Y. Zhang, H. Sagawa, D. Yoshino, K. Hagino, and J. Meng, Prog. Theor. Phys. **120**, 129 (2008).
[43] M. T. Win, K. Hagino, and T. Koike, Phys. Rev. C **83**, 014301 (2011).
[44] H. Sagawa, X. R. Zhou, X. Z. Zhang, and T. Suzuki, Phys. Rev. C **70**, 054316 (2004).
[45] J. Terasaki, P. H. Heenen, H. Flocard, and P. Bonche, Nucl. Phys. A **600**, 371 (1996).
[46] National Nuclear Data Center, https://www.nndc.bnl.gov/nudat3/.
[47] T. Motoba, H. Bandō, and K. Ikeda, Prog. Theor. Phys. **70**, 189 (1983).
[48] E. Hiyama, M. Kamimura, K. Miyazaki, and T. Motoba, Phys. Rev. C **59**, 2351 (1999).
[49] H.-J. Schulze, M. T. Win, K. Hagino, and H. Sagawa, Prog. Theor. Phys. **123**, 569 (2010).
[50] J. Yao, Z. Li, K. Hagino, M. Win, Y. Zhang, and J. Meng, Nucl. Phys. A **868–869**, 12 (2011).
[51] B.-N. Lu, E.-G. Zhao, and S.-G. Zhou, Phys. Rev. C **84**, 014328 (2011).
[52] D. Davis, Nucl. Phys. A **754**, 3 (2005).
[53] A. Gal, E. V. Hungerford, and D. J. Millener, Rev. Mod. Phys. **88**, 035004 (2016).
[54] M. Agnello *et al.*, Phys. Lett. B **622**, 35 (2005).
[55] M. Agnello *et al.*, Phys. Lett. B **698**, 219 (2011).
[56] Y. Funaki, Phys. Rev. C **92**, 021302(R) (2015).
[57] Y. Funaki, M. Isaka, E. Hiyama, T. Yamada, and K. Ikeda, Phys. Lett. B **773**, 336 (2017).
[58] C. Kurokawa and K. Katō, Phys. Rev. C **71**, 021301(R) (2005).
[59] C. Kurokawa and K. Katō, Nucl. Phys. A **792**, 87 (2007).
[60] S.-I. Ohtsubo, Y. Fukushima, M. Kamimura, and E. Hiyama, Prog. Theor. Exp. Phys. **2013**, 073D02 (2013).
[61] H. Horiuchi, Prog. Theor. Phys. **51**, 1266 (1974).
[62] Y. Funaki, A. Tohsaki, H. Horiuchi, P. Schuck, and G. Röpke, Phys. Rev. C **67**, 051306(R) (2003).
[63] A. S. Umar, K. Godbey, and C. Simenel, Phys. Rev. C **107**, 064605 (2023).
[64] J.-P. Ebran, E. Khan, T. Nikšić, and D. Vretenar, Nature (London) **487**, 341 (2012).
[65] J.-P. Ebran, E. Khan, T. Nikšić, and D. Vretenar, Phys. Rev. C **87**, 044307 (2013).
[66] J.-P. Ebran, E. Khan, T. Nikšić, and D. Vretenar, Phys. Rev. C **89**, 031303(R) (2014).
[67] N. Itagaki and E. Hiyama, Phys. Rev. C **107**, 024309 (2023).
[68] B. Zhou, A. Tohsaki, H. Horiuchi, and Z. Ren, Phys. Rev. C **94**, 044319 (2016).